Theoretical description of spontaneous pulse formation in a semiconductor microring laser

L. Gil*
Institut du Non Linéaire de Nice (Unité Mixte de Recherche–Centre National de la Recherche Scientifique 6618)
Université de Nice Sophia Antipolis, 1361 Route des Lucioles, F-06560 Valbonne, France

L. Columbo†
Consiglio Nazionale delle Ricerche–Istituto di Fotonica e Nanotecnologie,
Dipartimento Interuniversitario di Fisica, via Amendola, 173, 70126 Bari, Italy
(Received 11 October 2010; published 26 January 2011)

We theoretically describe the spontaneous formation of stable pulses in a GaAs bulk semiconductor microring laser. These pulses are obtained without active or passive mode locking. We show that the parameter regime associated with their existence is limited on one side by the phase instability of the continuous-wave solution, and on the other side by the failure of Lamb's mode-locking criterion. Bistability between the continuous-wave solution and the spontaneous pulses is observed.

DOI: 10.1103/PhysRevA.83.013822 PACS number(s): 42.55.Px, 42.60.Fc, 42.65.Pc

I. INTRODUCTION

Laser mode locking is a technique that generates ultrashort pulses for applications in metrology, optical communications, etc. [1,2]. In most cases, mode locking is obtained either by an external periodic modulation of a physical parameter with a frequency equal to the inverse of the resonator round trip time (active mode locking) or with the introduction of a saturable absorption inside the resonator (passive mode locking). Nonetheless, for certain applications it would be extremely interesting to deal with compact, monolithic devices emitting pulses via spontaneous (i.e., neither active nor passive) mode locking.

Lamb, in his pioneering contribution [3], derived an analytical criterion for a multimode laser to operate in the mode-locking regime. Afterwards, in the prototypical case of two level lasers but without any reference to Lamb's condition, Risken and Nummedal [4], Graham and Haken [5], and Narducci *et al.* [6] reported both theoretically and/or experimentally on the spontaneous formation of steady-state pulses in the regime of parameters where the continuous-wave (cw) solution is linearly unstable. More recently, Lamb's criterion has been extended to the more appealing case of a semiconductor bulk laser in a Fabry-Perot configuration [7] and used to demonstrate that this system also may exhibit stable mode-locked pulses. The authors reduce the full multimode dynamics to that of the three modes with the highest linear growth rate, compute the stationary solutions, and evaluate Lamb's condition in order to identify the parametric domain where the three modes are locked. After a careful reading of Ref. [7], we find it important to observe that (i) usually, taking into account additional modes strongly modifies the values of the stationary amplitudes of the three main modes and consequently Lamb's mode-locking condition; (ii) as we will show later in this paper, the accomplishment of Lamb's condition is necessary, but not sufficient, to guarantee pulse formation because it relates the phases of the competing modes and not their amplitudes. It turns out that in Ref. [7] the numerically measured amplitudes of the three phase locked modes are almost the same such that the output intensity presents the high contrast fluctuations characteristic of a pulse.

In this paper we report on the existence of stable high contrast, spontaneously formed, stable pulses in GaAs bulk semiconductor microring laser [8]. Our results have been obtained through an exact description of the multimode character of the dynamics. In particular, we show that the self-pulsing regime occurs in the parameters' subspace where both the continuous wave is linearly phase unstable and Lamb's condition is satisfied. Also, bistability between the continuous wave and the self-pulsing regimes is numerically observed.

We describe the longitudinal dynamics of a bulk semiconductor microring laser in the framework of the effective Maxwell-Bloch equations (EMBEs) [9]. The EMBEs are able to capture the essential features of the semiconductor gain and refractive index change with frequency and carriers density in a range of $\sim$10 THz around the gain peak. Furthermore, the application of the EMBEs to the propagation of picosecond pulses gives results in very good agreement with those of the full set of microscopic semiconductor Maxwell-Bloch equations as proved, for example, in Refs. [9–13]. For a larger interval of frequencies (which is not the case here), more sophisticated theoretical models of the semiconductor dynamics, including, for example, a more accurate description of the asymmetry of the susceptibility, are required [14,15].

The paper is organized as follows. In Sec. II, we derive the analytical expression of the continuous-wave solutions of the EMBEs and we perform their linear stability analysis, identifying the regime of parameters associated with 2,4, ... unstable adjacent cavity modes. In Sec. III, we first report on accurate numerical simulations in very good agreement with the analytical results of Sec. II. Then we describe the

*lionel.gil@inln.cnrs.fr
†lorenzo.columbo@gmail.com

spontaneous formation of picosecond pulses, with repetition rates of up to ∼1 THz, in the regime in which the phase instability [16] of the continuous waves is triggered by the first two unstable side modes. The self-starting pulses satisfy Lamb's condition and unavoidably lose stability when the number of unstable modes increases. Before concluding in Sec. V, we discuss in Sec. IV the possible consequences on self-starting pulses of some physical effects neglected in the EMBE model, and we mention some experimental evidences of spontaneous pulse formation in semiconductor lasers.

II. EFFECTIVE MAXWELL-BLOCH EQUATIONS

We consider a microring semiconductor laser in which the active medium, which is assumed to fill all of the cavity, is represented by a bulk GaAs sample. Transverse effects will be ignored in this paper.

We adopt the following notation for the slowly varying amplitudes of the electric field and the medium polarizations:

$$E = \tfrac{1}{2}(E^+ e^{i(k_r z-\omega_r t)} + E^- e^{i(-k_r z-\omega_r t)} + \text{c.c.}),$$
$$P = \tfrac{1}{2}(P^+ e^{i(k_r z-\omega_r t)} + P^- e^{i(-k_r z-\omega_r t)} + \text{c.c.}),$$

where z denotes the longitudinal coordinate, $k_r = \frac{\omega_r n_b}{c}$, n_b is the background refractive index, and ω_r is a reference frequency chosen arbitrarily. The effective Maxwell-Bloch equations read [9]

$$\frac{\partial E^+}{\partial t} = \frac{i\omega_r\Gamma_c}{2\epsilon_0 n_g n_b}P^+ + \frac{i\omega_r\Gamma_c\chi_0(N)n_b}{2n_g}E^+ - \frac{c}{n_g}\frac{\partial E^+}{\partial z}, \quad (1)$$

$$\frac{\partial E^-}{\partial t} = \frac{i\omega_r\Gamma_c}{2\epsilon_0 n_g n_b}P^- + \frac{i\omega_r\Gamma_c\chi_0(N)n_b}{2n_g}E^- + \frac{c}{n_g}\frac{\partial E^-}{\partial z}, \quad (2)$$

$$\frac{\partial P^+}{\partial t} = \{-\Gamma_0(N) + i[\delta_0 - \delta(N)]\}P^+ - i\epsilon_0\epsilon_b A(N)E^+, \quad (3)$$

$$\frac{\partial P^-}{\partial t} = \{-\Gamma_0(N) + i[\delta_0 - \delta(N)]\}P^- - i\epsilon_0\epsilon_b A(N)E^-, \quad (4)$$

$$\frac{\partial N}{\partial t} = D\frac{\partial^2 N}{\partial z^2} - \gamma(N - N_p) + \frac{i}{4\hbar}\{\epsilon_0\epsilon_b[\overline{\chi_0(N)} - \chi_0(N)] \times (|E^+|^2 + |E^-|^2) + \overline{P^+}E^+ - P^+\overline{E^+} + \overline{P^-}E^- - P^-\overline{E^-}\}, \quad (5)$$

where we introduced the confinement factor $\Gamma_c = 0.2376$, n_g is the so-called group index, $\epsilon_b = n_b^2$, δ_0 represents the difference between the reference frequency and $\omega_a = E_g/\hbar$, where E_g is the energy gap. The complex quantities χ_0 and the real ones Γ_0, δ, and A are functions of the carrier density N. Their detailed expressions depend on the semiconductor material and can be either computed from the microscopic theory or fitted from some experimental measurements [9]. In the equation for N, the parameter D represents the carrier diffusion coefficient and γ represents the carrier nonradiative decay time, while N_p is the pump parameter. The details about the derivation and the limitations of this model have been extensively discussed in Refs. [9,11,12].

Let us introduce $\langle\chi_{0r}\rangle = 0.13$ and $\langle N\rangle \simeq 10^{24}m^{-3}$ as the characteristic values of $\mathrm{Re}(\chi_0)$ and of N. With the following scalings,

$$\nu = \frac{\omega_r\Gamma_c\langle\chi_{0r}\rangle n_b}{n_g}, \quad E_r^2 = \frac{4\hbar\langle N\rangle\gamma}{\epsilon_0\epsilon_b}, \quad N = \langle N\rangle N',$$
$$\partial_t = \nu\partial_{t'}, \quad E^+ = E_r F, \quad D_{zz} = \frac{D\nu^2 n_g^2}{c^2\gamma},$$
$$\partial_z = \frac{\nu n_g}{c}\partial_{z'}, \quad E^- = E_r B, \quad (6)$$
$$\partial_x = \sqrt{\frac{2\omega_r n_b n_g \nu}{c^2}}\partial_{x'}, \quad P^+ = \epsilon_0\epsilon_b E_r P_F, \quad I_p = \frac{N_p}{\langle N\rangle},$$
$$\Gamma_0(N) = \nu\Gamma_0'(N'), \quad P^- = \epsilon_0\epsilon_b E_r P_B, \quad \gamma_{||} = \frac{\gamma}{\nu},$$
$$\delta_0 = \nu\delta_0', \quad \delta(N) = \nu\delta'(N'), \quad A(N) = \nu A'(N'),$$

the equations (1)–(5) take the adimensional form

$$\partial_t F = \frac{i}{\langle\chi_{0r}\rangle}P_F + \frac{i\chi_0(N)}{\langle\chi_{0r}\rangle}F - \partial_z F, \quad (7)$$

$$\partial_t B = \frac{i}{\langle\chi_{0r}\rangle}P_B + \frac{i\chi_0(N)}{\langle\chi_{0r}\rangle}B + \partial_z B, \quad (8)$$

$$\partial_t P_F = \{-\Gamma_0(N) + i[\delta_0 - \delta(N)]\}P_F - iA(N)F, \quad (9)$$

$$\partial_t P_B = \{-\Gamma_0(N) + i[\delta_0 - \delta(N)]\}P_B - iA(N)B, \quad (10)$$

$$\partial_t N = -\gamma_{||}\{N - I_p - D_{zz}\partial_{zz}N - 2\,\mathrm{Im}[\chi_0(\mathrm{N})](|\mathrm{F}|^2 + |\mathrm{B}|^2) - i(\overline{P_F}F - P_F\overline{F} + \overline{P_B}B - P_B\overline{B})\}, \quad (11)$$

where we dropped the primes on the new variables and we simplified the symbol of partial derivation.

Assuming a ring cavity configuration with $z \in [0, L]$, the boundary conditions are expressed as

$$F(0) = F(L)\rho e^{i\theta}, \qquad B(L) = B(0)\rho e^{i\theta}, \quad (12)$$

where $\theta = k_r L$ and ρ is the reflection coefficient linked to the transmission coefficient T by the relation $\rho = 1 - T$. Equations (7)–(11) , together with the boundary condition (12), form the set of equations that have been precisely numerically integrated.

A. Continuous-wave solutions and their linear stability analysis

In order to obtain a few analytical insights, some manipulations and assumptions are required. First, it is more convenient to work with periodic boundary conditions. We introduce the following change of variables:

$$F(t,z) = \mathcal{F}(t,z)e^{-az}, \quad P_F(t,z) = \mathcal{P}_\mathcal{F}(t,z)e^{-az},$$
$$B(t,z) = \mathcal{B}(t,z)e^{+az}, \quad P_B(t,z) = \mathcal{P}_\mathcal{B}(t,z)e^{+az}, \quad (13)$$

with $a = \frac{1}{L}[\ln(\rho) + i\theta]$. Equations (7)–(11) then become

$$\partial_t\mathcal{F} = \frac{i}{\langle\chi_{0r}\rangle}P_\mathcal{F} + \left(\frac{i\chi_0(N)}{\langle\chi_{0r}\rangle} + a\right)\mathcal{F} - \partial_z\mathcal{F}, \quad (14)$$

$$\partial_t\mathcal{B} = \frac{i}{\langle\chi_{0r}\rangle}P_\mathcal{B} + \left(\frac{i\chi_0(N)}{\langle\chi_{0r}\rangle} + a\right)\mathcal{B} + \partial_z\mathcal{B}, \quad (15)$$

$$\partial_t P_\mathcal{F} = \{-\Gamma_0(N) + i[\delta_0 - \delta(N)]\}P_\mathcal{F} - iA(N)\mathcal{F}, \quad (16)$$

$$\partial_t P_\mathcal{B} = \{-\Gamma_0(N) + i[\delta_0 - \delta(N)]\}P_\mathcal{B} - iA(N)\mathcal{B}, \quad (17)$$

$$\begin{aligned}\partial_t N = &-\gamma_{||}\{N - I_p - D_{zz}\partial_{zz}N - 2\,\mathrm{Im}[\chi_0(N)] \\ &\times (e^{-2\ln(\rho)z}|\mathcal{F}|^2 + e^{+2\ln(\rho)z}|\mathcal{B}|^2) \\ &- i e^{-2\ln(\rho)z}(\overline{P_\mathcal{F}}\mathcal{F} - P_\mathcal{F}\overline{\mathcal{F}}) \\ &- i e^{+2\ln(\rho)z}(\overline{P_\mathcal{B}}\mathcal{B} - P_\mathcal{B}\overline{\mathcal{B}})\},\end{aligned} \tag{18}$$

where $\mathcal{F}$ and $\mathcal{B}$ now satisfy the relations

$$\mathcal{F}(0) = \mathcal{F}(L), \qquad \mathcal{B}(L) = \mathcal{B}(0).$$

Furthermore, in the good cavity approximation ($\rho \longrightarrow 1$), we can greatly simplify the study of (14)–(18) by eliminating the explicit z dependences in the equation for N. This approximation is expected to be very well verified, for example, in the case of semiconductor resonators with Bragg mirrors. We finally obtain

$$\partial_t \mathcal{F} = \frac{i}{\langle\chi_{0r}\rangle} P_\mathcal{F} + \left(\frac{i\chi_0(N)}{\langle\chi_{0r}\rangle} + a\right)\mathcal{F} - \partial_z \mathcal{F}, \tag{19}$$

$$\partial_t \mathcal{B} = \frac{i}{\langle\chi_{0r}\rangle} P_\mathcal{B} + \left(\frac{i\chi_0(N)}{\langle\chi_{0r}\rangle} + a\right)\mathcal{B} + \partial_z \mathcal{B}, \tag{20}$$

$$\partial_t P_\mathcal{F} = \{-\Gamma_0(N) + i[\delta_0 - \delta(N)]\}P_\mathcal{F} - iA(N)\mathcal{F}, \tag{21}$$

$$\partial_t P_\mathcal{B} = \{-\Gamma_0(N) + i[\delta_0 - \delta(N)]\}P_\mathcal{B} - iA(N)\mathcal{B}, \tag{22}$$

$$\begin{aligned}\partial_t N = &-\gamma_{||}\{N - I_p - D_{zz}\partial_{zz}N - 2\,\mathrm{Im}[\chi_0(\mathrm{N})] \\ &\times (|\mathcal{F}|^2 + |\mathcal{B}|^2) - i(\overline{P_\mathcal{F}}\mathcal{F} - P_\mathcal{F}\overline{\mathcal{F}} + \overline{P_\mathcal{B}}\mathcal{B} - P_\mathcal{B}\overline{\mathcal{B}})\},\end{aligned} \tag{23}$$

with the boundary conditions

$$\mathcal{F}(0) = \mathcal{F}(L), \qquad \mathcal{B}(L) = \mathcal{B}(0).$$

We search for continuous-wave solutions of (19)–(23) in the form

$$\begin{aligned}\mathcal{F} = \mathcal{F}_0 e^{i(Kz-\Omega t)}, \quad P_\mathcal{F} = P_{\mathcal{F}_0} e^{i(Kz-\Omega t)}, \\ \mathcal{B} = \mathcal{B}_0 e^{i(-Kz-\Omega t)}, \quad P_\mathcal{B} = P_{\mathcal{B}_0} e^{i(-Kz-\Omega t)}, \\ N = N_0,\end{aligned} \tag{24}$$

where $\mathcal{F}_0$, $P_{\mathcal{F}_0}$, $\mathcal{B}_0$, and $P_{\mathcal{B}_0}$ are complex, while N_0, Ω, and K are real constants. After some trivial but long algebra,

$$\begin{aligned}K = \frac{2\pi n}{L}, n \in \mathcal{Z}, \quad I_0 = |\mathcal{F}_0|^2 + |\mathcal{B}_0|^2 = \frac{L\rho(I_p - N_0)}{\langle\chi_{0r}\rangle(1-\rho^2)}, \\ P_{\mathcal{F}_0} = \frac{-iA(N_0)\mathcal{F}_0}{i\Omega + \Gamma_0(N_0) + i[\delta(N_0) - \delta_0]}, \quad \Omega = \Omega(N_0, K), \\ P_{\mathcal{B}_0} = \frac{-iA(N_0)\mathcal{B}_0}{i\Omega + \Gamma_0(N_0) + i[\delta(N_0) - \delta_0]}, \quad \mathcal{E}(N_0, K) = 0,\end{aligned} \tag{25}$$

where $\mathcal{E}(N_0, K) = 0$ indicates a nonlinear equation in N_0 parametrized by K; its long and complex expression is given in the Appendix, together with that of Ω. For a given value of K, this equation implicitly defines the stationary carrier density value N_0 from which the corresponding values of $\mathcal{I}_0$, $\mathcal{P}_{\mathcal{F}_0}$, $\mathcal{P}_{\mathcal{B}_0}$, and Ω can be computed. The set of cw solutions is infinite and is parametrized by three continuous variables and one discrete variable. Among the three continuous variables, two are associated with the translation invariance of the EMBE with respect to time and space and are represented by the phases of the forward $\mathcal{F}_0$ and backward $\mathcal{B}_0$ electric field envelopes; the third is associated with the continuous distribution of the energy between forward and backward waves, with only the total intensity (I_0) being fixed. Finally, the discrete index (n) comes out from the constraint onto the wave vector K imposed by the periodic boundary conditions.

Figure 1 concerns the comparison between the cw analytical computations and the results of the numerical integration of (7)–(11). In particular, for a given value of n and for different values of the physical parameters L, θ, and I_p, we compare the total intensity I_0 given by (25) with the numerically computed spatially averaged intensity $I_{\mathrm{av}} = [\int_0^L (|F(z)|^2 + |B(z)|^2)dz]/L \simeq [\int_0^L (|\mathcal{F}(z)|^2 + |\mathcal{B}(z)|^2)\,dz]/L$. The very good quantitative agreement between the analytical predictions and the numerical observations justifies *a posteriori* the use of the good cavity approximation. It also gives us confidence in the study of the linear stability of the cw through the approximations (19)–(23).

We studied at this point the linear stability of the cw solutions with respect to spatially modulated perturbations by searching for solutions of Eqs (19)–(23) in the form

$$\begin{aligned}\mathcal{F} = (\mathcal{F}_0 + \delta\mathcal{F}e^{ikz}e^{\lambda t})e^{i(Kz-\Omega t)}, \\ \mathcal{P}_\mathcal{F} = (\mathcal{P}_{\mathcal{F}_0} + \delta\mathcal{P}_\mathcal{F}e^{ikz}e^{\lambda t})e^{i(Kz-\Omega t)}, \\ \mathcal{B} = (\mathcal{B}_0 + \delta\mathcal{B}e^{-ikz}e^{\lambda t})e^{i(-Kz-\Omega t)}, \\ \mathcal{P}_\mathcal{B} = (\mathcal{P}_{\mathcal{B}_0} + \delta\mathcal{P}_\mathcal{B}e^{-ikz}e^{\lambda t})e^{i(-Kz-\Omega t)}, \\ N = N_0 + \delta N e^{ikz}e^{\lambda t},\end{aligned} \tag{26}$$

and by numerically solving the nonlinear characteristic equation for the complex eigenvalues $\lambda(k)$. We show in Fig. 2 typical plots of the highest growth rate [$\mathrm{Re}(\lambda)$] of the perturbation versus its associated spatial Fourier component k. The shape of the curves is a clear signature of the phase instability regime [16]. The different curves correspond to different values of the ratio between the forward and the backward field amplitudes. Even if, as we already pointed out, the energy repartition is continuous between pure traveling cw ($|F| = 0$ or $|B| = 0$, top curve) and pure standing cw ($|F| = |B|$, bottom curve), only a finite number of curves has been plotted. In addition, we note that the standing wave is always the most stable. Finally, in order to be able to plot the continuous lines in Fig. 2, we consider k as a continuous variable, but only the discrete values $k_j = 2\pi j/L$, $j \in \mathcal{Z}$ are consistent with the boundary conditions. In the following, a cw solution will be defined as unstable when it corresponds to unstable traveling and standing waves.

We make the following observations: (i) A modulational instability can affect the cw solution only for values of the cavity length L higher than $L_c = 2\pi/k_c$, where k_c is the critical key vector shown in Fig. 2. (ii) By keeping fixed the other parameters, we can increase the number of unstable modes k_j and then the complexity of the system spatiotemporal behavior, by simply considering longer cavities [even if, according to (25), by changing L we also slightly change the cw solution that we are considering]. The usual experimental accessible parameter I_p also controls the number of unstable modes, but it also modifies some intrinsic laser characteristics such

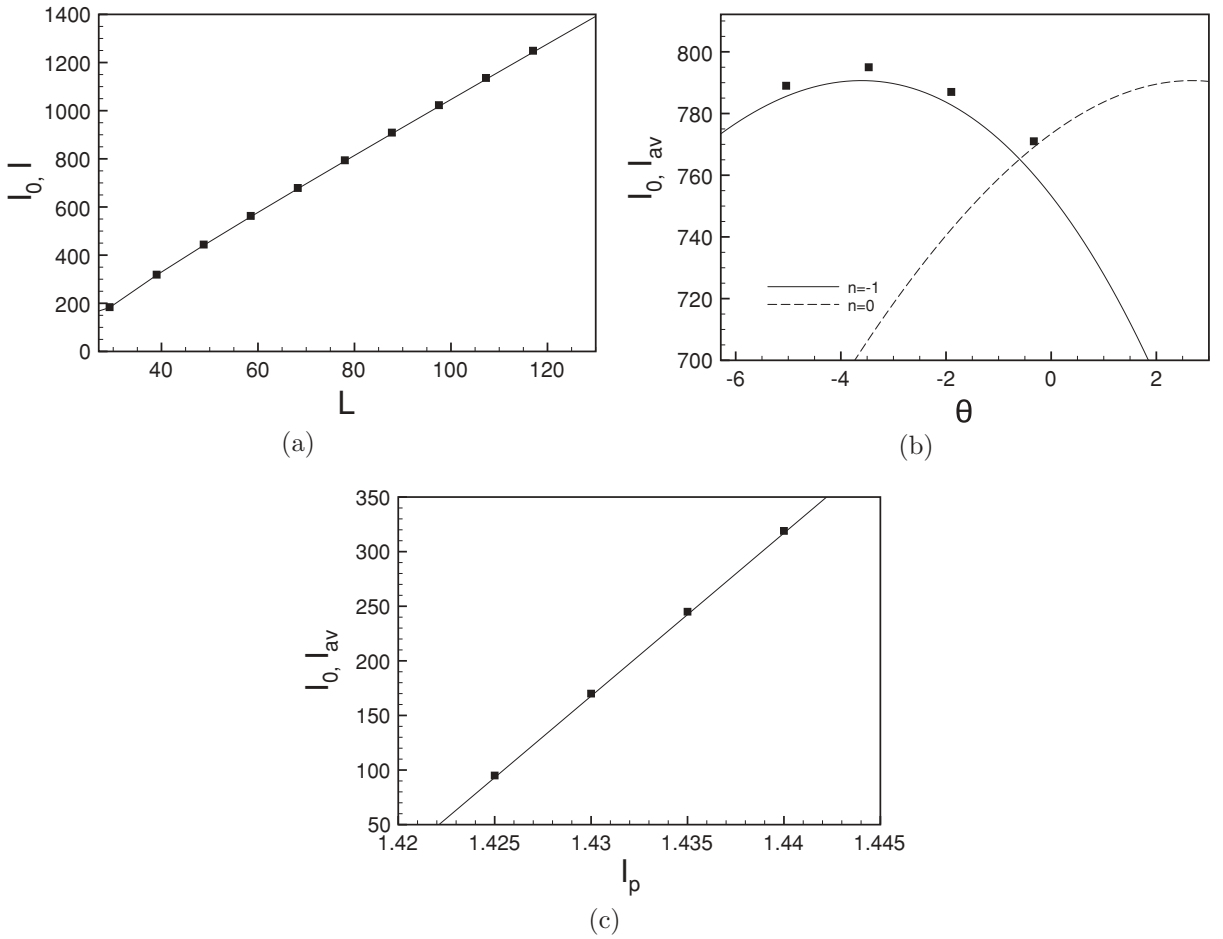

FIG. 1. Quantities I_0 (continuous line) and I_{av} (square symbols) calculated, respectively, from relations (25) and by numerical integration of Eqs (7)–(11) plotted for different values of (a) the cavity length L ($n = -1$, $I_p = 1.44$, and $\theta = -3.47$), (b) the cavity detuning θ ($I_p = 1.44$ and $L = 97.5$), and (c) the pump I_p ($n = -1$, $\theta = -3.47$, and $L = 39$). The other parameters are $\rho = 0.99$, $\gamma_{\parallel} = 2 \times 10^{-5}$, $D_{zz} = 0.0$, and $\delta_0 = 0$.

as the central frequency or the full width at half maximum (FWHM) of the gain curve through $\Gamma_0(N)$ and $\delta(N)$. For these reasons, we decided to use L (instead of I_p) as our main control parameter.

III. SPONTANEOUS FORMATION OF PULSES

In order to study the dynamics in the parametric regimes in which the cw solutions are unstable, we performed a set of simulations by numerically integrating Eqs (7)–(11) and the boundary conditions (12) for an increasing number of unstable side modes. Even if we mainly used an efficient and accurate split-step scheme based on a combination of Runge-Kutta and fast Fourier transform algorithms, we also adopted a completely different numerical scheme, based on finite differences, to check the most relevant results of our simulations and to investigate the effect of more complex boundary conditions.

We started to consider the situation in which only the two side modes $K + k_{\pm 1}$ are unstable ($L_c < L < 2L_c$). Depending on the parameters, we observed the following.

(i) Low amplitude modulations of the uniform cw solution (we call this solution acw for almost cw). In this case, the amplitude in the Fourier spectrum of the side modes $K + k_{\pm 1}$ is orders of magnitude smaller than that of the spatial frequency K.

(ii) Steady-state pulses in both the forward and the backward field, which propagate in the cavity with constant velocity, constant shape, and high contrast (Fig. 3). In this case the three adjacent modes have almost the same amplitude.

(iii) Irregular oscillations in the field intensity.

As emphasized in Ref. [8], the pulse formation in case (ii) is due to a spontaneous mode-locking phenomenon: It results neither from a modulation of the cavity losses (or of some other parameter) by means of an external forcing, nor from a coupling between the active medium and a saturable absorber inside the cavity. The spontaneously formed pulses are characterized by a temporal resolution of $\sim$1 ps and a repetition rate of up to $\sim$1 THz. Although the first value is quite far from the frontier ($\sim$10 fs) [1], the very high pulse repetition rate makes the compact device we considered very appealing for the realization of optical interconnections, optical clocks, and also new devices for biological metrology, etc. [1,2]. On the basis of this remarkable result, the Centre National de la Recherche Scientifique (France) applied for a patent [17].

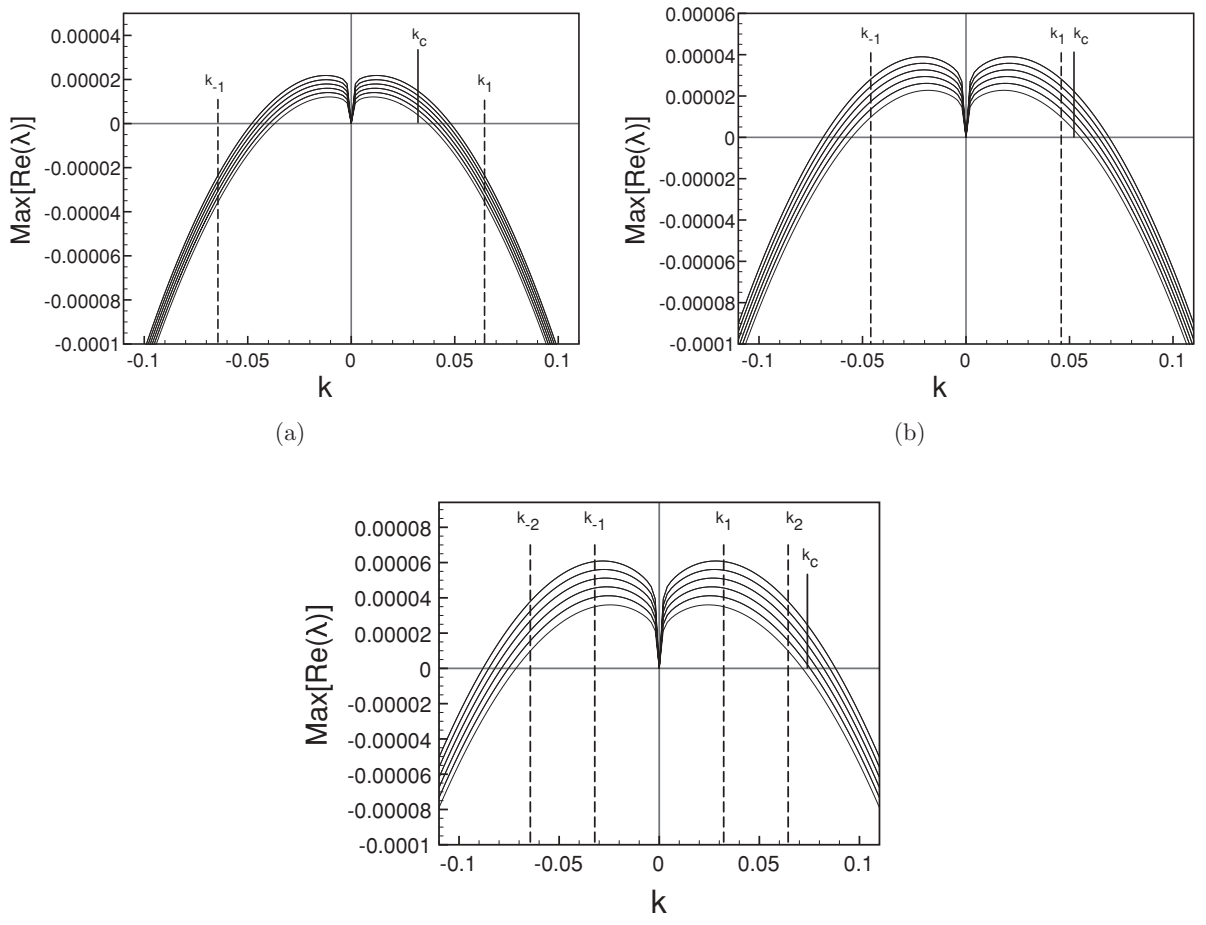

FIG. 2. Linear stability analysis of the cw solutions. We focus on the most unstable cw solution that corresponds to $n = -1$. The plot displays the highest growth rate [Re(λ)] versus the wave number k. k_c denotes the critical key vector. The different curves correspond to different values of the ratio $|\mathcal{F}_0|/|\mathcal{B}_0|$. The most stable solution corresponds to the pure standing wave ($|\mathcal{F}_0| = |\mathcal{B}_0|$), while the most unstable solution corresponds to the pure traveling wave ($|F| = 0$ or $|B| = 0$). By varying the cavity length, we pass from zero unstable modes (vertical dashed lines) for $L = 97.5$ (a), to two and then four unstable modes, respectively, for $L = 136.5$ (b) and $L = 195$ (c). The other parameters are $\theta = -3.47$, $I_p = 1.44$, $\rho = 0.99$, $\gamma_\parallel = 2 \times 10^{-5}$, $D_{zz} = 0.0$, and $\delta_0 = 0$.

When $L > 2L_c$, the next two side modes $K + k_{\pm 2}$ become linearly unstable. This leads, in all of the considered cases, to the destabilization of the pulse solution. In particular, for increasing values of L, we observed a transition between a field intensity profile characterized by one or two irregular pulses (not constant shape and velocity) (see Fig. 4) and a more complex spatiotemporal behavior.

In the (θ, L) plane of Fig. 5, we summarize the whole set of our numerical results. The dashed and the continuous lines represent, respectively, the analytically computed functions $L = L_c(\theta)$ and $L = 2L_c(\theta)$. Despite its not-so-high resolution, due to the very time-consuming character of the numerical simulations, Fig. 5 gives a reasonable sketch of the system phase diagram.

In all of the cases reported in Fig. 5, the transitions between the cw or acw solutions and the self-starting pulses are undoubtedly second order. However, this is not always the case, and subcritical transitions giving rise to bistability between pulses and cw (or acw) solutions can be obtained for smaller values of L and higher values of I_p [8] (see Fig. 6). This bistable behavior, together with the compactness and simplicity of the semiconductor device, could turn out to have possible applications to all optical information storage and processing.

The last part of this section concerns Lamb's mode-locking criterion. In the neighborhood of a cw solution, in the case in which only the adjacent modes $K + k_{\pm 1}$ are unstable, we obtain for the forward field

$$\mathcal{F}(t,z) \simeq [A_0(t) + A_+(t)e^{i(k_1 z)} + A_-(t)e^{i(k_{-1} z)}] \times e^{i(Kz - \Omega t)},$$

where A_0 is the complex amplitude of the K mode, and $A_{+,-}$ are those of the two adjacent modes. By writing $A_{0,+,-}(t) = |A_{0,+,-}(t)|e^{i\phi_{0,+,-}(t)}$, it turns out that the moduli $|A_{0,+,-}|$ and the relative phase difference $\Delta = \phi_+ + \phi_- - 2\phi_0$ form an invariant subspace for the dynamics. The equation for Δ is [3]

$$\partial_t \Delta = \alpha[\beta - \sin(\Delta - \Delta_0)], \tag{27}$$

where α, β, and Δ_0, depending on $|A_{0,+,-}|$, are in general functions of time. When Lamb's condition ($|\beta| < 1$) is

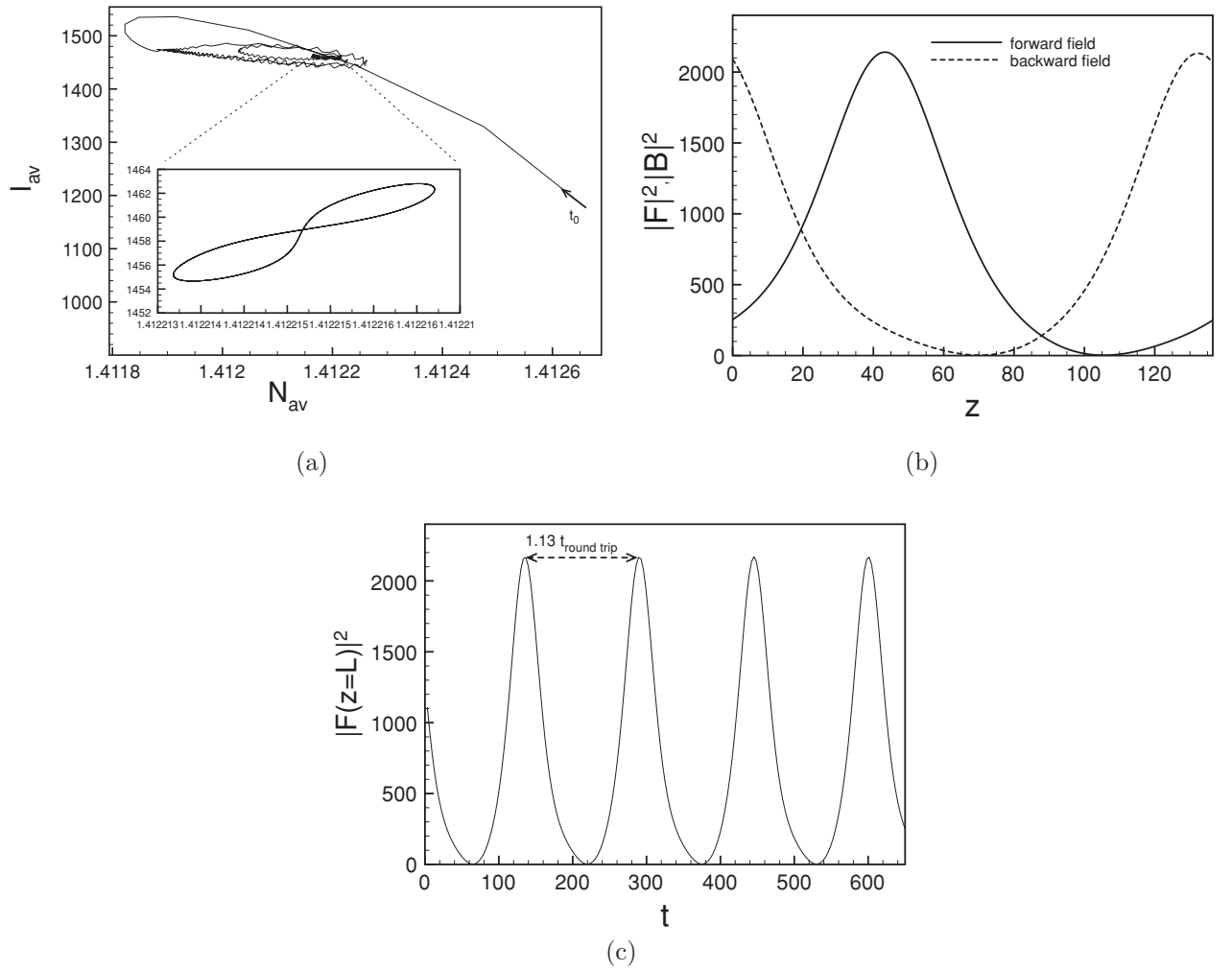

FIG. 3. $L = 136.5$, regular pulsing regime: (a) Temporal evolution in the $(N_{\rm av}, I_{\rm av})$ plane. $I_{\rm av}$ is defined in the text, and $N_{\rm av}$ stands for the average along z of the carrier density. t_0 is the starting point, and the arrow indicates the temporal evolution direction. The inset is a closeup of the asymptotic regime. (b) Longitudinal profile of the forward and backward field intensities corresponding to a stable pulse. The contrast is remarkably high. (c) Intensity of the forward field for $z = L$ vs time. The optical pulse travels in the resonator with a constant width and a constant velocity slightly smaller than the velocity of light in the medium (=1 in scaled units). The other parameters are $\theta = -3.47$, $I_p = 1.44$, $\rho = 0.99$, $\gamma_\parallel = 2 \times 10^{-5}$, $D_{zz} = 0.0$, and $\delta_0 = 0$.

verified, Eq. (27) admits two fixed points, one stable and one unstable; the former corresponds to a phase-locked solution. We numerically computed the quantity $\zeta = \frac{A_- A_+ \bar{A}_0^{\,2}}{|A_-||A_+||A_0|^2} = e^{i\Delta}$ and plotted its real part versus time for different parametric regimes. Note that, differently from what was done in Ref. [7], the quantity ζ is computed from the full set of equations (7)–(11). The results obtained for three different cases are shown in Fig. 7. One temporal trace strongly fluctuates between -1 and $+1$ and then is clearly associated with an unlocked regime. It corresponds to an irregular oscillations regime similar to that in Fig. 4. The other two curves, being almost constant in time, satisfy Lamb's criterion. The more regular one is associated with a self-starting pulse, while the other one is associated with an acw solution. This latter evidence reveals that (i) the accomplishment of Lamb's mode-locking condition is necessary, but not sufficient, for the observation of pulses in the intensity field profile; (ii) the parameter regime associated with the existence of pulses is limited on one side by the phase instability of the continuous-wave solutions, and on the other side by the failure of Lamb's mode-locking criterion.

IV. DISCUSSION

A. Grating effect in a bidirectional ring resonator

In the EMBE (7)–(11) description of a bidirectional resonator, the carrier density spatial grating due to the interference between the two counterpropagating fields has been neglected. This approximation is usual for semiconductors. Physically, it can be considered valid because typical carrier diffusion rates for conduction-band electrons wash out such a "fast" (half the optical wavelength) grating. In any case, we want to emphasize that the existence of two counterpropagating waves is not a necessary condition for the observation of stable pulses. To check this, we run some simulations in a unidirectional ring cavity and we still observed the spontaneous formation of pulses in the resonator.

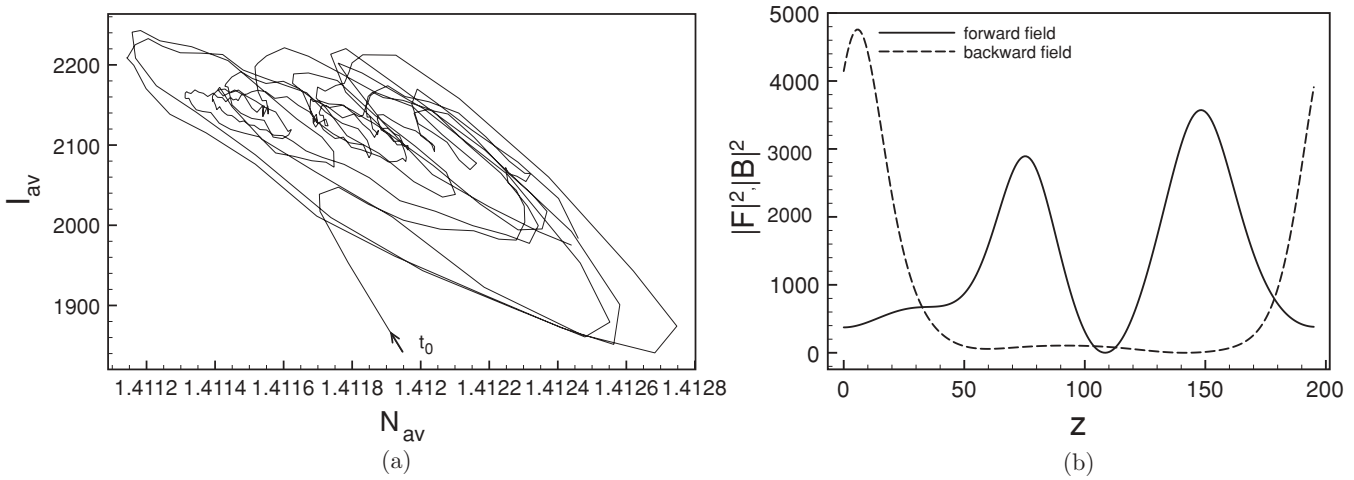

FIG. 4. $L = 195$, irregular pulsing regime: (a) Temporal evolution in the $(N_{\rm av}, I_{\rm av})$ plane. (b) Longitudinal profile of the forward and backward field intensities after $\sim 10^6$ time units ($\sim 5 \times 10^3$ cavity round trips) showing irregular intensity oscillations. The other parameters are $\theta = -3.47$, $I_p = 1.44$, $\rho = 0.99$, $\gamma_\parallel = 2 \times 10^{-5}$, $D_{zz} = 0.0$, and $\delta_0 = 0$.

B. Effect of the use of a more realistic resonator configuration on the pulse formation and stability

Usually the ring configuration allows for a deeper analytical investigation than the Fabry-Perot (FP) configuration, which is in turn more relevant from a practical point of view. Our case does not represent an exception: We succeeded in obtaining analytical and accurate expressions of the continuous waves in both configurations, but we managed to perform the linear stability analysis only in the ring configuration and we resorted to numerical simulations for the FP case. In particular, we found stable cw solutions, but surprisingly we did not observe any kind of stable pulse solution. For long enough cavities (or for high enough values of the pump), the cw solution becomes unstable and gives rise to strong modulation of the electric field amplitude. Throughout the temporal evolution, it often happens that the intensity profile approaches the pulse shape for a few round trips. However, due to the nonvanishing reflection, several secondary pulses are emitted from the boundaries, interact with the main pulse, and always prevent the field intensity from converging to a stationary configuration.

Even if, in the FP configuration, we did not run so huge a series of simulations as in the ring resonator case, and consequently our numerical investigations may not be considered exhaustive, the results we obtained somehow suggest an unwanted destabilization mechanism associated with the existence of back reflections. Because the boundary conditions (12) are only an idealization, one may wonder if the pulse in the ring configuration will persist in the presence of a small back reflection such as, for example, at the interface between the nonlinear active medium and the dielectric region that fills the rest of the cavity. To answer such a question, we numerically investigated the geometry sketched in Fig. 8. The region with length L_1 corresponds to the semiconductor. In this nonlinear region, the density of carriers, the polarization, and the electric fields obey Eqs (7)–(11). In the linear dielectric

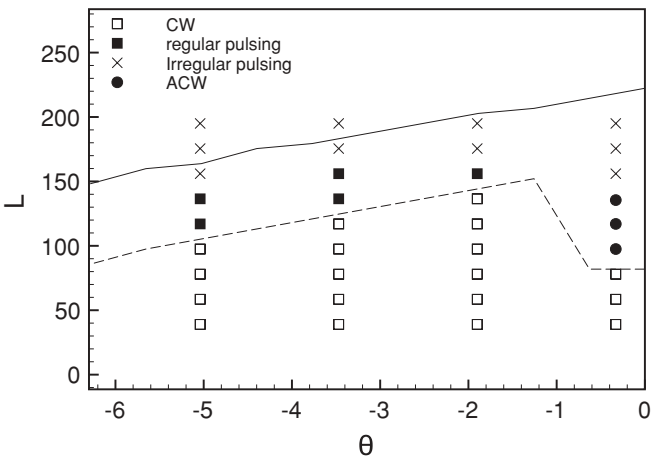

FIG. 5. Phase diagram of Eqs (7)–(11) in the (θ, L) plane for $I_p = 1.44$. The other parameters are $I_p = 1.44$, $\rho = 0.99$, $\gamma_\parallel = 2 \times 10^{-5}$, $D_{zz} = 0.0$, and $\delta_0 = 0$.

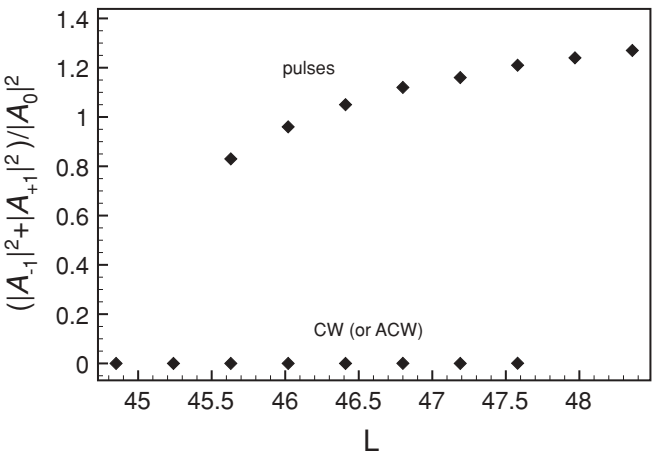

FIG. 6. Normalized amplitudes of the side modes $K + k_{\pm 1}$ vs L. $I_p = 2.06$, $\theta = -3.47$, $\rho = 0.99$, $\gamma_\parallel = 2 \times 10^{-5}$, $D_{zz} = 1.2$, and $\delta_0 = 0$. The upper branch corresponds to the pulse solution, while the lower branch corresponds to the cw (or acw) solution.

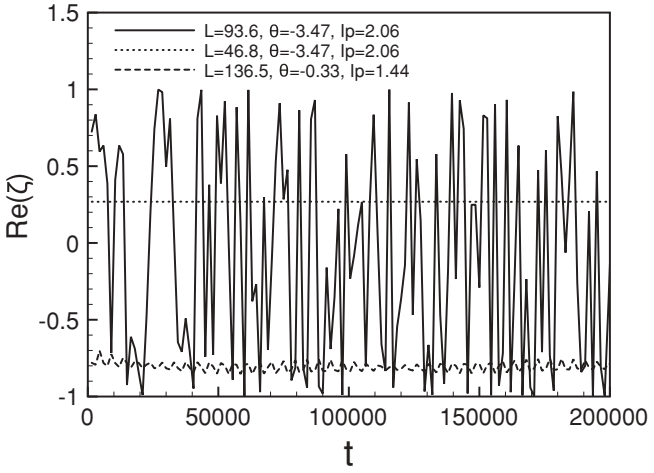

FIG. 7. Real part of the quantity ζ vs time for different dynamical configurations: irregular pulsing (continuous line), steady-state pulses (dotted line), and acw solution (dashed line). The parameters not indicated in the figure are $\rho = 0.99$, $\gamma_{\parallel} = 2 \times 10^{-5}$, $D_{zz} = 1.2$, and $\delta_0 = 0$.

region (with length L_2), the electric field obeys

$$n_2^2 \frac{\partial^2 E_2}{\partial t^2} = -\frac{\sigma_2}{\epsilon_0}\frac{\partial E_2}{\partial t} + c^2 \frac{\partial^2 E_2}{\partial z^2}, \tag{28}$$

where n_2 is the real refractive index and σ_2 stands for linear losses. Around the reference frequency ω_r, we may write E_2 in the form

$$E_2 = \tfrac{1}{2}\left(E_2^+ e^{i(k_2 z - \omega_r t)} + E_2^- e^{i(-k_2 z - \omega_r t)}\right) + \text{c.c.}, \tag{29}$$

where $k_2 = n_2\omega_r/c$. In the slowly varying envelope approximation, the amplitudes $E_2^{\pm}$ obey

$$\frac{\partial E_2^+}{\partial t} = \frac{-\sigma_2}{2\epsilon_0 n_2^2} E_2^+ - \frac{c}{n_2}\frac{\partial E_2^+}{\partial z},$$
$$\frac{\partial E_2^-}{\partial t} = \frac{-\sigma_2}{2\epsilon_0 n_2^2} E_2^- + \frac{c}{n_2}\frac{\partial E_2^-}{\partial z}.$$

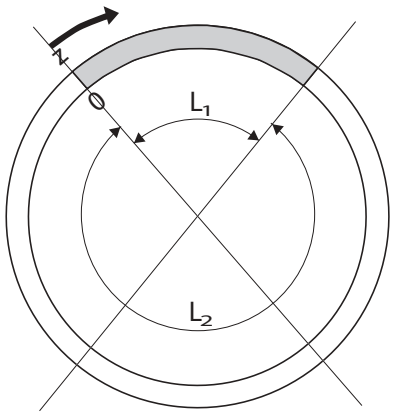

FIG. 8. Schematic description of a ring cavity partially filled by the active medium. The semiconductor is placed in the region with length L_1, while L_2 corresponds to a linear dielectric with no dispersion and with a n_2 refraction index.

With the scalings (6), we are then left with

$$\frac{\partial F_2}{\partial t} = -\frac{\mu}{n_2^2} F_2 - \frac{n_g}{n_2}\frac{\partial F_2}{\partial z}, \tag{30}$$
$$\frac{\partial B_2}{\partial t} = -\frac{\mu}{n_2^2} B_2 + \frac{n_g}{n_2}\frac{\partial B_2}{\partial z}, \tag{31}$$

with $\mu = \frac{\sigma_2}{2\epsilon_0 \nu}$.

At $z = 0$ and $z = L_1$, the continuity of the electric field (E) and its first-order spatial derivative ($\frac{\partial E}{\partial z}$) must be imposed. In computing ($\frac{\partial E}{\partial z}$), we neglected the spatial variation of the amplitudes in front of that of the electric-field phase, in such a way that the boundary conditions can be expressed, as usual, in terms of reflection and transmission coefficients. These complex coefficients depend on k_r and k_2 and therefore on ω_r, whose choice is arbitrary. This may lead to the following systematic mistake: Let us assume that, in order to start the simulation, we use $\omega_r = \omega_a$ to compute the numerical values of the coefficients in Eqs (7)–(11) and the reflection and transmission coefficients in $z = 0$ and $z = L_1$. Then if the electric field frequencies ω_s, which are selected by the system during its evolution, are not equal to ω_a, there is an error associated with the computation of the reflection and transmission coefficients. This error depends on the difference $\omega_s - \omega_r$ and is expected to be small because $\frac{\omega_s - \omega_r}{\omega_r} \ll 1$. We note, also, that there exist some numerical techniques to deal with this problem in an exact way, but they are unfortunately associated with a very high computational load. Here, we tried to minimize the error by choosing the transparency frequency as the reference frequency. We checked that the results of the simulations are consistent with this assumption. Figure 9 summarizes our main numerical results. The simulation running times are expressed in rescaled units and correspond to $\simeq$103 round trips. When the amplitude of the forward electric wave at $z = L_1$ reaches a maximum or a minimum, the values of these extrema together with their time of occurrence are recorded. In the figure we plot the values of these extrema versus time. The curves appear to be continuous because of the long running time of the observation but are in fact discrete. We also observed a well-defined time periodicity (relative fluctuations are $<0.1\%$) associated with the time needed for the pulse to perform a round trip. Figure 9(b), where the maximum and minimum converge to the same value, corresponds to the cw regime, while Figs. 9(a) and 9(c), showing a steady high contrast between maximum and minimum, are associated with the pulsing regime. Several remarks are in order:

(i) The behavior of the backward electric field is strictly analogous to that of the forward one. In the case of the cw regime, the spatial average amplitudes are the same, and in the pulsing regime, the forward and backward pulses have the same amplitude and width.

(ii) The pulse is self-starting.

(iii) Small white noise fluctuations around vanishing polarization and electric fields have been used as initial conditions. For the carrier density, we start with small fluctuations around the transparency value. Also, for each given regime of parameters, the time evolution was investigated with five distinct initial conditions. In this way we checked that the asymptotic regimes (cw solution or self-pulsing) do not depend on the initial conditions.

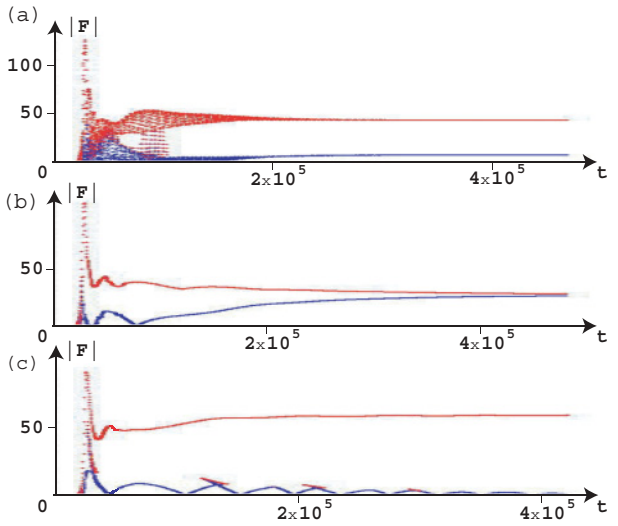

FIG. 9. (Color online) Numerical simulation of Eqs (7)–(11) and (30) with the geometrical configuration described in Fig. 8. The plots display the successive local maximum (upper red curve) and minimum (lower blue curve) of the amplitude of the forward electric field at $z = L_1$ versus time (see description in the text). The curves are discontinuous but may look like continuos when the value of the extremum slowly changes with time. Fig. 9(a) and Fig. 9(c) are clearly associated with the pulsing regime while Fig. 9(b) corresponds to the cw regime. Parametric regime: $n_b = 3.6$, $n_g = 4.6$, $\mu = 0.05$, $I_p = 1.6$, $D_{zz} = 1.2$, $\gamma_{\parallel} = 2 \times 10^{-5}$, $\sigma = 0$, $\delta_0 = 0.35247$, $L_1 = 102.3$, and $n_2 = 3.0$. L_2 is, respectively, equal to 15.548 (a) 15.563 (b) and 15.579 (c).

(iv) The only difference among the three plots in Fig. 9 is the value L_2 used in the simulation. Even if we are not able to give an exact explication of the huge sensitivity to the length L_2, we can mention that such a sensitivity can be proved in the quite similar case of the propagation of a gap soliton in a nonlinear periodic medium.

C. Experimental evidences of self-pulsing in semiconductor lasers and their theoretical interpretations

From an experimental point of view, the existence of self-starting pulses in semiconductor lasers has been reported in Refs. [7,18–20]. Apart, perhaps, from the case already discussed of Ref. [7], there is not, so far, a robust theoretical interpretation of these results. In Ref. [18] the authors give an interpretation of their results in terms of Kerr-Lens self-mode locking and part of their motivation is that "there is no evidence of any alternative self-mode locking mechanism". In Refs. [19,20], the authors simply suggest the four-wave mixing in the gain section, whose efficiency is enhanced in discrete level systems, as the major phenomenon leading to mode locking.

Although there are some differences in the type of semiconductor active medium (bulk instead of quantum dots, quantum dashes, or quantum cascade) as well as in the geometrical configurations (ring instead of FP), we think that the understanding of the previous experimental observations might benefit from our theoretical results. At least now, another self-mode-locking mechanism is conceivable.

V. CONCLUSION

We identified the regime of existence of steady-state self-starting pulses in a semiconductor microring laser. To address this issue, we studied the longitudinal multimode system dynamics in the theoretical framework of the effective semiconductor Maxwell-Bloch equations. In the regime of parameters in which only two resonant side modes drive the continuous-wave solution phase instability, we observed the spontaneous formation of stable picosecond pulses traveling in the resonator with constant speed, constant shape, and a repetition rate of up to ∼1 THz. We verified that these solutions satisfy Lamb's mode-locking criterion, exist in a sizable interval of the control parameter represented in our case by the cavity length, and can be bistable with the continuous waves. When the number of phase unstable modes increases, the pulse solutions lose their stability and the system evolves toward a regime of irregular pulsations.

Finally, we think that our results could help to interpret some recent experimental observations of self-mode locking in semiconductor lasers and to stimulate new experimental investigations of this phenomenon.

ACKNOWLEDGMENTS

The greater part of this work has been carried out in the framework of the European STREP project 004868 named FUNFACS (Fundamentals, Functionalities and Applications of Cavity Solitons). We acknowledge J. Tredicce, S. Barland, and P. Genevet for useful discussions.

APPENDIX

We report the explicit expressions of the frequency Ω and of the nonlinear equation that defines the stationary values of the carrier density N_0 in (25):

$$\begin{aligned}\Omega &= \Omega(N_0, K)\\ &= \{\Gamma_0(N_0)[KL\langle\chi_{0r}\rangle + \langle\chi_{0r}\rangle\theta + L\chi_{0r}(N_0)]\\ &\quad +[\langle\chi_{0r}\rangle \ln(\rho) - L\chi_{0i}(N_0)][\delta(N_0) - \delta_0]\}\\ &\quad /L\langle\chi_{0r}\rangle\,\Gamma_0(N_0) - \langle\chi_{0r}\rangle\,\ln(\rho) + L\chi_{0i}(N_0),\end{aligned}$$

where χ_{0r} and χ_{0i} denote, respectively, the real and the imaginary part of χ,

$$\begin{aligned}&\mathcal{E}(N_0, K) = 0 \Longleftrightarrow\\ &(c_{32}K^2 + c_{31}K + c_{30})L^3 + (c_{22}K^2 + c_{21}K + c_{20})L^2\\ &\quad +(c_{11}K + c10)L + c_{00} = 0,\end{aligned}$$

with

$$c_{32} = \langle\chi_{0r}\rangle^2\Gamma_0(N_0)\chi_{0i}(N_0),$$
$$c_{31} = -2\,\langle\chi_{0r}\rangle\,\Gamma_0(N_0)\chi_{0i}(N_0)[\langle\chi_{0r}\rangle\,\delta_0 - \langle\chi_{0r}\rangle\,\delta(N_0) - \chi_{0r}(N_0)],$$

$$
\begin{aligned}
c_{30} = {} & \langle\chi_{0r}\rangle^2\delta(N_0)^2\chi_{0i}(N_0)\Gamma_0(N_0) + \chi_{0i}(N_0)^3\Gamma_0(N_0) + \langle\chi_{0r}\rangle^2\delta_0{}^2\chi_{0i}(N_0)\Gamma_0(N_0) - A(N_0)\langle\chi_{0r}\rangle^2\Gamma_0(N_0)^2 \\
& - 2\,\langle\chi_{0r}\rangle^2\delta(N_0)\chi_{0i}(N_0)\delta_0\,\Gamma_0(N_0) - 2\,\chi_{0r}(N_0)\chi_{0i}(N_0)\delta_0\,\langle\chi_{0r}\rangle\,\Gamma_0(N_0) + 2\,\chi_{0i}(N_0)^2\Gamma_0(N_0)^2\langle\chi_{0r}\rangle \\
& - 2\,A(N_0)\langle\chi_{0r}\rangle\,\Gamma_0(N_0)\chi_{0i}(N_0) - A(N_0)\chi_{0i}(N_0)^2 + 2\,\chi_{0r}(N_0)\chi_{0i}(N_0)\delta(N_0)\langle\chi_{0r}\rangle\,\Gamma_0(N_0) \\
& + \chi_{0r}(N_0)^2\Gamma_0(N_0)\chi_{0i}(N_0) + \chi_{0i}(N_0)\Gamma_0(N_0)^3\langle\chi_{0r}\rangle^2,
\end{aligned}
$$

$$
\begin{aligned}
c_{22} &= -\langle\chi_{0r}\rangle^3\Gamma_0(N_0)\ln(\rho), \\
c_{21} &= 2\,\langle\chi_{0r}\rangle^2\Gamma_0(N_0)[-\chi_{0r}(N_0)\ln(\rho) + \langle\chi_{0r}\rangle\ln(\rho)\delta_0 - \langle\chi_{0r}\rangle\ln(\rho)\delta(\mathrm{N_0}) + \theta\,\chi_{0i}(\mathrm{N_0})], \\
c_{20} = {} & -\langle\chi_{0r}\rangle[4\,\langle\chi_{0r}\rangle\ln(\rho)\Gamma_0(N_0)^2\chi_{0i}(N_0) + \langle\chi_{0r}\rangle^2\delta_0{}^2\ln(\rho)\Gamma_0(N_0) + 2\,\langle\chi_{0r}\rangle\,\theta\,\Gamma_0(N_0)\chi_{0i}(N_0)\delta_0 \\
& + \langle\chi_{0r}\rangle^2\delta(N_0)^2\ln(\rho)\Gamma_0(N_0) + 2\,\chi_{0r}(N_0)\langle\chi_{0r}\rangle\ln(\rho)\delta(N_0)\Gamma_0(N_0) - 2\,\langle\chi_{0r}\rangle^2\delta(N_0)\ln(\rho)\delta_0\,\Gamma_0(N_0) \\
& - 2\,\chi_{0r}(N_0)\theta\,\Gamma_0(N_0)\chi_{0i}(N_0) + 3\ln(\rho)\Gamma_0(N_0)\chi_{0i}(N_0)^2 - 2\,A(N_0)\langle\chi_{0r}\rangle\,\Gamma_0(N_0)\ln(\rho) + \chi_{0r}(N_0)^2\Gamma_0(N_0)\ln(\rho) \\
& - 2\chi_{0r}(N_0)\langle\chi_{0r}\rangle\ln(\rho)\delta_0\,\Gamma_0(N_0) - 2\,\langle\chi_{0r}\rangle\,\theta\,\delta(N_0)\Gamma_0(N_0)\chi_{0i}(N_0) + \langle\chi_{0r}\rangle^2\ln(\rho)\Gamma_0(N_0)^3 - 2\,A(N_0)\ln(\rho)\chi_{0i}(N_0)],
\end{aligned}
$$

$$
\begin{aligned}
c_{11} &= -2\,\langle\chi_{0r}\rangle^3\theta\,\Gamma_0(N_0)\ln(\rho), \\
c_{10} &= \langle\chi_{0r}\rangle^2[2\,\langle\chi_{0r}\rangle\ln(\rho)^2\Gamma_0(N_0)^2 + 2\,\langle\chi_{0r}\rangle\,\theta\,\Gamma_0(N_0)\ln(\rho)\delta_0 - A(N_0)\ln(\rho)^2 \\
& \quad + 3\ln(\rho)^2\Gamma_0(N_0)\chi_{0i}(N_0) + \theta^2\Gamma_0(N_0)\chi_{0i}(N_0) - 2\,\langle\chi_{0r}\rangle\,\theta\,\delta(N_0)\Gamma_0(N_0)\ln(\rho)], \\
c_{00} &= -\langle\chi_{0r}\rangle^3\Gamma_0(N_0)\ln(\rho)[\ln(\rho)^2 + \theta^2].
\end{aligned}
$$

[1] U. Keller, Nature (London) **424**, 831 (2003).
[2] J. C. Diels and W. Rudolph, *Ultrashort Laser Pulse Phenomena* (Elsevier, New York, 2006).
[3] W. E. Lamb, Phys. Rev. **134**, A1429 (1964).
[4] H. Risken and K. Nummedal, J. Appl. Phys. **39**, 4662 (1968).
[5] R. Graham and H. Haken, Z. Phys. **213**, 420 (1968).
[6] L. M. Narducci, J. R. Tredicce, L. A. Lugiato, N. B. Abraham, and D. K. Bandy, Phys. Rev. A **33**, 1842 (1986).
[7] Y. Nomura, S. Ochi, N. Tomita, K. Akiyama, T. Isu, T. Takiguchi, and H. Higuchi, Phys. Rev. A **65**, 043807 (2002).
[8] L. Columbo and L. Gil, Opt. Lett. **35**, 1473 (2010).
[9] C. Z. Ning, R. A. Indik, and J. V. Moloney, IEEE J. Quantum Electron. **33**, 1543 (1997).
[10] J. V. Moloney, R. A. Indik, and C. Z. Ning, IEEE Photonics Technol. Lett. **9**, 731 (1997).
[11] C. Z. Ning, J. V. Moloney, A. Egan, and R. A. Indik, Quantum Semiclass. Opt. **9**, 681 (1997).
[12] C. Z. Ning and P. M. Goorjian, J. Opt. Soc. Am. B **16**, 2072 (1999).
[13] M. Bahl, H. Rao, N. C. Panoiu, and R. M. Osgood Jr., Opt. Lett. **29**, 1689 (2004).
[14] J. Yao, G. P. Agrawal, P. Gallion, and C. M. Bowden, Opt. Commun. **119**, 246 (1995).
[15] J. Javaloyes and S. Balle, IEEE J. Quantum Electron. **45**, 431 (2009).
[16] T. B. Benjamin and J. E. Feir, J. Fluid Mech. **27**, 417 (1967).
[17] L. Gil and L. Columbo, *Fonctionnement d'un laser micro-anneau en régime impulsionel*, Centre National de la Recherche Scientifique and Université de Nice-Sophia Antipolis patent application ref. 08/06123 (3 November 2008).
[18] R. Paiella, F. Capasso, C. Gmachl, D. L. Sivco, J. N. Baillargeon, A. L. Hutchinson, A. Y. Cho, and H. C. Liu, Science **290**, 1739 (2000).
[19] J. Renaudier *et al.*, Elect. Lett. **41**, 1007 (2005).
[20] C. Gosset, K. Merghem, A. Martinez, G. Moreau, G. Patriarche, G. Aubin, A. Ramdane, J. Landreau, and F. Lelarge, Appl. Phys. Lett. **88**, 241105 (2006).